C. R. Geoscience 343 (2011) 210–218

Contents lists available at ScienceDirect

Comptes Rendus Geoscience

www.sciencedirect.com

Petrology, geochemistry (Mineralogy)

Composition and structural aspects of naturally occurring ferrihydrite

Composition et propriétés structurales des ferrihydrites naturelles

A. Cristina Cismasu [a,*], F. Marc Michel [a,b], A. Patricia Tcaciuc [c], Tolek Tyliszczak [d], Gordon E. Brown, Jr [a,b,e]

[a] *Department of Geological and Environmental Sciences, Stanford University, Stanford CA 94305-2115, USA*
[b] *Stanford Synchrotron Radiation Lightsource, SLAC National Accelerator Laboratory, 2575 Sand Hill Rd, MS 69, Menlo Park, CA 94025, USA*
[c] *Woods Hole Oceanographic Institution, Massachusetts Institute of Technology, Cambridge, MA 02139-4307, USA*
[d] *Chemical Sciences Division, Lawrence Berkeley National Laboratory, Berkeley, CA 94720, USA*
[e] *Department of Photon Science, SLAC National Accelerator Laboratory, 2575 Sand Hill Rd, MS 69, Menlo Park, CA 94025, USA*

ARTICLE INFO

Article history:
Received 30 October 2010
Accepted after revision 17 November 2010

Mots clés :
Ferrihydrite
Composition
Structure
Réactivité

Keywords:
Ferrihydrite
Composition
Structure
Reactivity

ABSTRACT

A series of naturally occurring ferrihydrites sampled from an acid mine drainage environment were characterized and compared with synthetic 2-line ferrihydrite using high energy X-ray total scattering and pair distribution function analysis, Scanning Transmission X-ray Microscopy (STXM), Transmission Electron Microscopy (TEM), BET N_2 surface area measurements, and chemical extractions in order to place constraints on their structural and physical properties as a function of composition. Overall, the short- and intermediate-range ordering of the natural samples is comparable to synthetic ferrihydrite. However, with increasing Al, Si, and organic matter contents, a decrease in particle size and an increase in structural disorder were observed. Silica is suspected to have a pronounced effect on the crystallinity of ferrihydrite as a result of its inhibitory effect on Fe polymerization and particle growth, and it is likely complexed at the surfaces of ferrihydrite nanoparticles. Aluminum, on the other hand may substitute for Fe^{3+} in natural ferrihydrite. Organic matter is pervasive and intimately associated with ferrihydrite aggregates, and its presence during ferrihydrite precipitation may have contributed to additional structural disorder. The increase in impurity content affects not only the particle size and structural order of ferrihydrite but may also have a significant effect on its surface reactivity.

RÉSUMÉ

Une série de ferrihydrites naturelles provenant d'un site de drainage minier acide a été caractérisée et comparée à une ferrihydrite synthétique « *2-line* » par diffraction des rayons-X (DRX), microscopie à balayage par transmission de rayons-X (STXM), microscopie électronique à transmission (MET), analyses BET N_2 et extractions chimiques, pour étudier l'impact de la composition chimique sur les propriétés physiques et structurales de ce minéral. Globalement, la structure des ferrihydrites naturelles est similaire à celle de la ferrihydrite synthétique. Cependant, une augmentation des teneurs en Al, Si, et matière organique associées avec la ferrihydrite, entraîne une baisse de la taille des particules et une augmentation du désordre structural. Ces changements ont été attribués principalement à la présence du silicium, qui affecte de manière significative la

* Corresponding author.
E-mail address: cismasu@stanford.edu (A.C. Cismasu).

1631-0713/$ – see front matter
doi:10.1016/j.crte.2010.11.001

polymérization du fer en solution, la cristallinité et la croissance des particules. Le silicium serait plutôt complexé à la surface des nanoparticules de ferrihydrite, tandis que l'aluminium pourrait être incorporé dans la structure même des ferrihydrites. Une forte association entre la matière organique et la ferrihydrite a été observée et on soupçonne que sa présence, lors de la précipitation de ferrihydrite, a aussi affecté le désordre structural de ces matériaux. La présence de ces impuretés pourrait également fortement modifier la réactivité de surface des ferrihydrites naturelles.

1. Introduction

Ferrihydrite is a hydrated Fe(III) nano-oxide that is ubiquitous in various Earth surface environments. Due to its abundance, frequent occurrence as particle coatings, and its large reactive surface area resulting from its small particle size (1–7 nm), ferrihydrite is well recognized for its capacity to control the mobility of inorganic and organic pollutants in the environment through sorption reactions. Its occurrence is documented at near-neutral pH conditions in a variety of redox-active environments, such as soils and sediments, as well as freshwater and marine settings (Jambor and Dutrizac, 1998 and references therein), where it may comprise a considerable fraction of the available reactive surface area. Ferrihydrite can also be found locally in vast sedimentary deposits in environments characterized by high ferrous iron supply from groundwaters and high oxidation rates. Well-known examples of such settings include acid mine drainage (AMD) environments, ferriferous groundwater springs, hydrothermal springs, and seafloor vents (Boyd and Scott, 1999; Carlson and Schwertmann, 1981; Childs et al., 1982; Kim and Kim, 2003; Pichler et al., 1999). In several of these settings, an accelerated oxidation of iron by microbial activity was shown to be favorable (Ferris et al., 1989; Kennedy et al., 2003) but not essential for ferrihydrite precipitation.

The complexity of naturally occurring ferrihydrite is attributed not only to its poor crystallinity and nanoparticulate character but also to considerable variations in its composition. Several inorganic impurities including aluminum, silicon, arsenic, manganese, phosphorous, as well as natural organic matter (NOM) are known to be associated with ferrihydrite as a result of their affinity for iron oxides. For example, precipitates from AMD environments, volcanic springs, and cold springs were found to contain between 0.5 and 31.5 wt % SiO_2, between 0.5 to 9.6 wt % Al_2O_3, and up to 7.2 wt % PO_4 (Boyd and Scott, 1999; Childs et al., 1982; Henmi et al., 1980; Jambor and Dutrizac, 1998; Kim and Kim, 2003; Parfitt et al., 1992). Arsenic is particularly abundant in ferrihydrites formed in acid mine drainage environments as well as in some isolated hydrothermal deposits, with reported As(V) contents between 0.7 and 28.3 wt % (Majzlan et al., 2007; Pichler et al., 1999). The association of NOM with iron precipitates has also been documented in instances where such precipitates form under the influence of bacterial cells or bacterial exudates in hydrothermal, lacustrine, and AMD settings (Chan et al., 2004; Fortin et al., 1993; Kennedy et al., 2003). Furthermore, correlations between carbon and iron contents in soils have led to suggestions that there is an intimate association between humic substances and nanoparticulate iron oxyhydroxides (Schwertmann et al., 2005).

These impurity species can affect ferrihydrite crystallinity and particle size, its solubility and stability with respect to transformation, its aggregation properties, as well as its surface structure and composition. These changes in its physicochemical properties can also impact ferrihydrite chemical reactivity significantly and in variable ways. Several studies on doped synthetic ferrihydrites have shown that the presence of foreign ions and/or organic molecules can affect ferrihydrite reactivity with respect to reductive dissolution (Jentzsch and Penn, 2006), siderophore-promoted dissolution (Mikutta and Kretzschmar, 2008), and metal(loid) adsorption (Anderson and Benjamin, 1985; Anderson and Benjamin, 1990; Masue et al., 2007). Thus, a knowledge of the structure, composition, and physical properties of naturally occurring ferrihydrite is important for understanding its reactivity in the environment. Despite numerous studies of naturally occurring ferrihydrites, detailed information on their atomic-level structures is lacking. Indeed, even the structure of synthetic ferrihydrite (Michel et al., 2007a; Michel et al., 2007b; Michel et al., 2010) has been the subject of significant debate (Combes et al., 1989; Combes et al., 1990; Drits et al., 1993; Manceau, 2009; Manceau, 2010; Rancourt and Meunier, 2008). Difficulties associated with the characterization of the structure and composition of this phase arise primarily from its nanometer-sized particles, inherent structural disorder, and lack of a crystalline counterpart. Recently, Michel et al. used X-ray total scattering and pair distribution function (PDF) analysis to propose a structural model describing synthetic ferrihydrite as a single defective phase (Michel et al., 2007a; Michel et al., 2010).

Variations in the composition of ferrihydrite are expected to have a direct effect on its structure. However, precise determination of natural ferrihydrite composition is often complicated by the formation of separate but intimately mixed nano-scale phases. The interaction of foreign species with ferrihydrite can range from structural incorporation to surface complexation and/or surface precipitation to physical mixtures at the nm scale. For example, cations with a similar valence state and ionic radius may substitute for Fe^{3+} and reside directly in the structure (Tang et al., 2010). Conversely, strong-binding ligands such as arsenate or silicate are suspected to be primarily associated with the surfaces of ferrihydrite particles as a result of their inhibitory effect on iron polymerization (Doelsch et al., 2000; Pokrovski et al., 2003; Waychunas et al., 1993). However, the distinction between

true chemical substitution and surface complexation is, in most cases, very difficult to make for these poorly crystalline nano-scale phases using conventional diffraction, imaging, and spectroscopic techniques. In some cases (e.g., Si impurities at high concentrations), available evidence suggests a physical association of ferrihydrite with a silica-rich phase(s), as will be discussed below.

In this study we have characterized a suite of naturally occurring Al-, Si-, and NOM-bearing ferrihydrites in an attempt to identify the effects of these impurity species on their structural and physical properties. We have compared our structural results for natural ferrihydrites with those from recent X-ray scattering studies of synthetic 2-line, 6-line (Michel et al., 2007a, 2007b), and ordered ferrihydrite (Michel et al., 2010). Ferrihydrite samples were collected from an AMD system at the New Idria mercury mine in central California. Their characterization was carried out using synchrotron-based (X-ray total scattering and PDF analysis, scanning transmission X-ray microscopy) and laboratory-based techniques (TEM, BET, ICP-AES), which provided atomic-scale structural information at short- and intermediate-ranges (~20 Å), evidence for compositional heterogeneity at the nm-scale, as well as clues about the effects of composition on particle size, aggregation properties, and the surface chemistry of natural ferrihydrites.

2. Materials and methods

Ferrihydrite was sampled at the New Idria mercury mine (San Benito Co., CA, USA), which was North America's second largest mercury producer located in the central part of the California Coast Range mercury mineral belt (Rytuba, 2000), where an AMD system has developed since the mine's closure in 1972. Three ferrihydrite samples, referred to as NIFh1, NIFh2, and NIFh3, were collected over a two-year period from the top few centimeters of the thick ferrihydrite sediment layer precipitated in the near-neutral pH waters of San Carlos Creek, which drains from the mine site. Once in the laboratory, the ferrihydrite slurries were centrifuged to separate excess water, dried in a fume hood and stored as powders. It is possible that centrifugation causes aggregation of ferrihydrite particles, although it is likely that they are already aggregated to some extent prior to centrifugation in part because of their small surface charge. The measured pH_{pzc} of the natural ferrihydrite samples (including impurities) varies between ~8 and 8.4 and thus the particles would be expected to have a near-neutral charge, which should lead to aggregation at the pH conditions of this site (pH = ~8). Pure synthetic ferrihydrite used for comparison with the natural samples was synthesized in the laboratory by neutralizing a 0.2 M ferric nitrate solution by 1 M NaOH to a pH value of 7.5, following the protocol developed by Schwertmann and Cornell (1991).

Chemical compositions of the natural ferrihydrites were obtained by ammonium oxalate extraction (Loeppert and Inskeep, 1996). This extraction procedure provides the composition of the poorly crystalline sample fraction and does not take into account the contribution of trace amounts of crystalline detrital phases such as quartz or clay minerals associated with the bulk sediment. All solutions obtained by digestion were filtered prior to analysis by ICP-AES (IRIS Advantage/1000 Radial ICAP Spectrometer). Weight loss on ignition was measured by heating the sample to 500 ± 50 °C for 4 hours. Total carbon and total organic carbon were measured by flash combustion with a Carlo-Erba NA 1500 analyzer; the organic carbon fraction was estimated by measuring ferrihydrite carbon contents after a weak acid wash (Midwood and Boutton, 1998).

BET N_2 surface area measurements were carried out using a Micromeritics ASAP 2020 surface area analyzer. Samples were degassed for 13 hours at a temperature of 50 °C before N_2 adsorption. TEM images were obtained using an FEI Tecnai G2 F20 X-TWIN TEM operating at 200 kV.

Scanning transmission X-ray microscopy (STXM) element mapping and near-edge X-ray absorption fine structure (NEXAFS) spectroscopy were performed at the Advanced Light Source (Lawrence Berkeley National Laboratory, Berkeley, CA, USA) on branch line 11.0.2.2. See Bluhm et al. (2006) for a detailed description of this beamline. Protocols for data acquisition and processing can be found in Bluhm et al. (2006) and Hitchcock (2001). Energy calibration for the C K-edge was performed using gaseous CO_2; quartz and gibbsite were used for Si K-edge and Al K-edge energy calibrations, respectively. All measurements were performed using a 25 nm Fresnel zone plate, which yielded a maximum spatial resolution of 25–30 nm. Samples were prepared by placing a drop of dilute ferrihydrite suspension onto either a lacey carbon-coated 300 mesh copper grid or a silicon nitride membrane. Elemental maps for Fe, Al, Si, and C were obtained by subtracting images taken at energies below the absorption edge of the element of interest from images taken at an energy slightly above the absorption edge. Carbon K-edge NEXAFS spectra were extracted from regions of interest on image stacks. Aluminum and silicon concentrations were not sufficient in the iron-rich portions of these samples to obtain good quality NEXAFS spectra. The aXis2000 software package was used for image and spectra processing (Hitchcock, 2000).

X-ray scattering data were collected at the Advanced Photon Source (Argonne National Laboratory) on beam line 11-ID-B. For these measurements, dry ferrihydrite powders were packed and sealed in 1 mm Kapton capillaries. A minimum of three replicates were prepared for each sample. Data were collected using either a MAR345 image plate detector or a Perkin Elmer amorphous silicon detector. An energy of ~90.5 keV (λ = 0.1372 Å) was used for wide-angle measurements. Low-angle diffraction data were collected to obtain high-resolution diffraction patterns in the low-Q region; a larger sample-to-detector distance was chosen for this experimental setup, and an energy of ~60 keV, (λ = 0.212 Å) was used. Calibration of sample-to-detector distances was performed using a CeO_2 standard. Integration of the raw scattering data into spectra was done using the Fit2D software (Hammersley, 1998), and a polarization correction was applied during the integration procedure. Diffraction spots resulting from the

presence of crystalline phases were masked prior to the integration step. This procedure is used to remove similar types of parasitic scattering in total scattering investigations using high-pressure cell devices (Ehm et al., 2007) and does not significantly affect the PDFs presented here. For each sample, we selected PDF data obtained from the purest sample fractions in order to avoid artifacts that result from the presence of crystalline phases. The total scattering structure function S(Q) and the pair distribution function G(r) were obtained using the program PDFgetX2 (Qiu et al., 2004). Data were initially normalized using the chemical composition of each individual sample, to obtain the total scattering structure function or S(Q). PDFs were obtained by Fourier transforming S(Q), with $Q_{max} = 22$ Å^{-1}. Standard corrections, as well as corrections typical for the image-plate geometry, were applied during data processing (Chupas et al., 2003).

3. Results and discussion

3.1. Composition of the New Idria ferrihydrites

The compositions of the poorly crystalline fraction of the New Idria precipitates are given in Table 1. Iron, aluminum, and silicon dominate in all three samples, and an increase in Al and Si contents was observed from sample NIFh1 to NIFh3. Other elements such as Mn, Mg, P, Ni, and Zn were found in amounts below 1 wt % and do not appear to follow a specific trend within the ferrihydrite suite examined. Water contents (adsorbed and structural) are significant and varied between 18 and 29.6 wt %. Although the values given in Table 1 represent a good approximation of the ferrihydrite compositions, it is unlikely that they provide an accurate composition of the ferrihydrite *sensu stricto*. Additional considerations must be taken into account when evaluating the results of this chemical extraction. Firstly, species associated with ferrihydrite as a result of sorption reactions that occurred during or subsequent to its formation may not necessarily be part of the crystal structure (e.g., surface precipitates). Secondly, as will be discussed below, these samples appear heterogeneous in composition and were found to contain individual, nm-scale Al- and/or Si-containing phases, which may also be dissolved by the ammonium oxalate extraction procedure in addition to ferrihydrite, resulting in an overestimation of the actual Al and Si contents of the ferrihydrite.

Fe, Al, and Si elemental maps were collected by STXM in order to visually inspect the spatial distribution of these elements. The maximum spatial resolution of the STXM microscope (25 nm for the setup conditions used here) was not sufficient to evaluate the distribution of Al and Si within ferrihydrite particles that are ~2 nm in size. Nevertheless, at the highest spatial resolution allowed, Al and Si were found to be intimately associated with ferrihydrite aggregates. However, in some cases, a speckled distribution of Al and Si was observed within ferrihydrite aggregates, which indicates that individual Al- and Si-rich phases ~100 to 200 nm in size are intermixed with ferrihydrite particles (Fig. 1). The nature of these nm-size

Table 1
Composition of the poorly crystalline fraction of the New Idria samples obtained by ammonium oxalate extraction; the contribution of trace silicate minerals (NIFh1, NIFh2, NIFh3) and calcite (NIFh3) is not taken into account for these analyses. Loss on ignition weight percentages as well as total and organic C wt % were estimated from bulk samples.

Tableau 1
Composition de la fraction mal cristallisée des échantillons de New Idria, obtenue par extraction a l'oxalate d'ammonium; la contribution des traces de phases cristallines silicatées (NIFh1, NIFh2, NIFh3) et de calcite (NIFh3) n'a pas été prise en compte pour ces analyses. La quantité d'eau structurale et adsorbée (*loss on ignition* = perte au feu), ainsi que la quantité de carbone total et organique ont été estimées à partir de l'échantillon brut.

wt %	NIFh1	NIFh2	NIFh3
SiO_2	2.59	7.20	9.07
Al_2O_3	4.80	8.87	15.04
Fe_2O_3	56.92	50.35	40.62
MnO	0.11	0.07	0.48
MgO	0.17	0.07	0.65
CaO	0.03	0.04	0.04
Na_2O	0.00	0.16	0.01
K_2O	0.01	0.28	0.02
P_2O_5	0.06	0.01	0.10
NiO	0.05	0.04	0.11
ZnO	0.11	0.16	0.63
Total C	0.78	1.33	2.13
Organic C	0.36	0.59	1.36
Loss on ignition	18.05	28.53	29.63

phases could not be determined directly by STXM as a result of their small particle sizes. However, Al K-edge NEXAFS data collected on larger, micron-size Al-rich regions indicated spectroscopic signatures typical for amorphous Al-hydroxide precipitates (data not shown). Additional crystalline aluminosilicate phases such as clays and albite were identified by Al-K edge NEXAFS (data not shown) and X-ray diffraction (see section 3.3), but their presence within ferrihydrite aggregates such as shown in Fig. 1 is not supported by our STXM elemental maps since overall there are no clear correlations between Al and Si hotspots. We suspect that these nano-scale hotspots correspond to Al-hydroxides and amorphous silica precipitates, which likely formed as a result of a heterogeneous precipitation process due to differences in the hydrolysis/aqueous chemistry of Al, Si and Fe, as well as reaction kinetics. A fraction of Al and Si may also be intimately associated with ferrihydrite particles through chemical substitution (Al), formation of surface complexes or surface precipitates (Si), and these possibilities will be discussed in section *3.3*.

STXM imaging also shows a strong correlation between iron and carbon (Fig. 2a). Estimated values for organic carbon in the New Idria samples vary from ~0.4 to 1.4 wt % (Table 1). Although these values are not particularly high, STXM maps indicate that carbon in the form of NOM is pervasive and appears to act as a matrix in which aggregates are embedded. Carbon K-edge NEXAFS spectra indicate a fairly similar carbon signature for all three samples (Fig. 2b). Functional groups in these spectra were identified by comparison with various literature reference spectra of organic and inorganic compounds (Benzerara et al., 2004; Schumacher et al., 2005; Solomon et al., 2009). We assigned the peak at 285 eV to the presence of aromatic

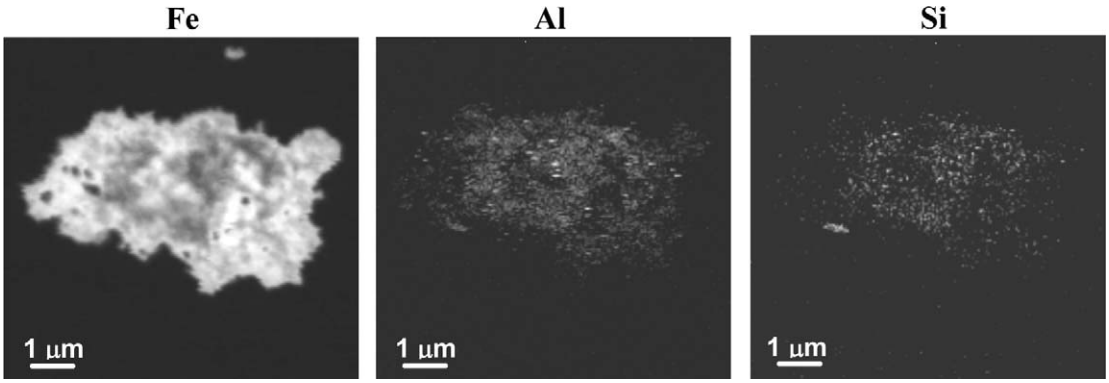

Fig. 1. Example of Fe, Al and Si Scanning Transmission X-ray Microscopy elemental maps of a ferrihydrite aggregate (sample NIFh3), showing compositional heterogeneity illustrated by speckled Al and Si distribution; Al-and Si-rich domains of ~100–200 nm in diameter are observed.

Fig. 1. Exemple de cartes de distribution de Fe, Al, et Si, obtenues par microscopie X en transmission par balayage pour un agrégat de ferrihydrite (échantillon NIFh3), montrant une hétérogénéité de composition à l'échelle submicronique; les zones enrichies en Al ou Si observées peuvent atteindre ~100 à 200 nm.

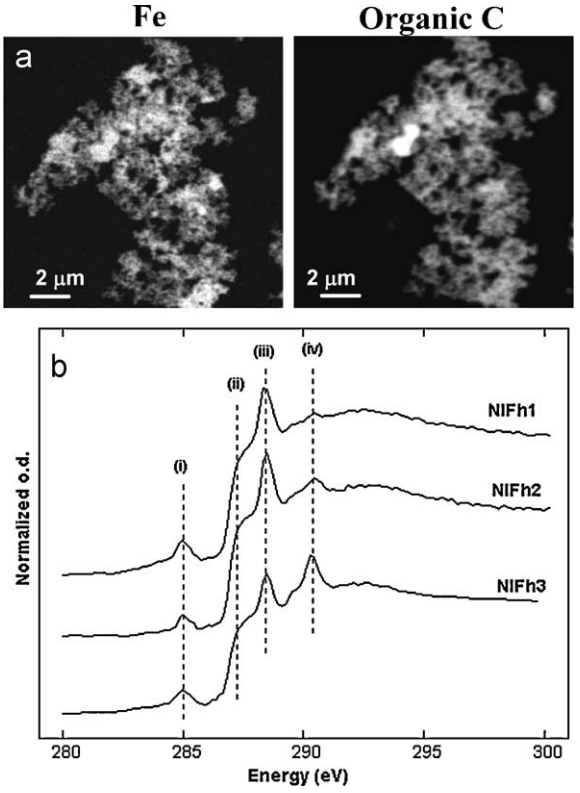

Fig. 2. (a) Fe and organic C Scanning Transmission X-ray Microscopy maps (sample NIFh3) indicate a close association of organic matter with ferrihydrite aggregates; (b) C K-edge NEXAFS spectra obtained from stacks for samples NIFh1, NIFh2 and NIFh3 indicate a fairly similar carbon signature in all three samples. Spectral features marked by dashed lines indicate (i) aromatic (285 eV), (ii) aliphatic (287.2 eV), (iii) carboxylic/peptidic (288.4 eV), and (iv) carbonate (290.4 eV) functional groups.

Fig. 2. (a) Cartes obtenues par microscopie X en transmission par balayage pour les agrégats de Fe, et C organique montrant une association forte entre ferrihydrite et la matière organique ; (b) spectres NEXAFS obtenus au seuil K du carbone pour les échantillons NIFh1, NIFh2 et NIFh3 montrant une signature similaire du carbone dans les trois échantillons étudiés. Les lignes pointillées indiquent les différents groupes fonctionnels identifiés correspondant à : (i) groupes aromatiques (285 eV), (ii) groupes aliphatiques (287,2 eV), (iii) groupes carboxyliques/peptidiques (288,4 eV) et (iv) carbonate (290,4 eV).

functional groups; the shoulder at 287.2 eV was assigned to aliphatic functional groups, and the slightly broadened peak at 288.4 eV was attributed to the presence of both carboxylic (~288.6 eV), and peptidic (288.2 eV) bonds. The presence of carboxyl and peptidic bonds implies the presence of polysaccharides and proteins respectively (Benzerara et al., 2004), indicating that the NOM may be of bacterial origin. Carbonate was identified in samples NIFh2 and NIFh3 only, based on the feature at 290.4 eV.

3.2. Aggregation, surface area and particle size

TEM images (Fig. 3) indicate that the New Idria ferrihydrites are found as rounded aggregates that vary in size from ~50 to 300 nm. Aggregate size decreases from sample NIFh1 to NIFh3. The smallest aggregates (NIFh3) are dense in appearance, suggesting a close packing of very small particles in comparison with the larger aggregates, in which particles appear to be slightly larger, and more loosely bound (NIFh1, NIFh2). These aggregates are thought to be representative of the natural samples prior to drying and centrifugation due to their small surface charge (see Section 2), and the difference in density of particle packing shown in Fig. 3 may be due to an aging or ripening effect. The measured BET surface area was found to be highest for sample NIFh1 (312 m^2/g) and lowest for sample NIFh3 (65 m^2/g), with the surface area of sample NIFh2 being intermediate (170 m^2/g). Although aggregates in sample NIFh1 are largest, and normally should have the smallest surface area, we expect that additional surface area is exposed as a result of the more loose packing of ferrihydrite particles. In contrast, particles in sample NIFh3 appear to be densely packed, and aggregates have nearly smooth edges. We suspect that the BET surface area measurements reflect to some extent the degree of packing of the ferrihydrite particles within aggregates, and not the overall aggregate sizes.

Individual ferrihydrite particles were identified at aggregate edges primarily for samples NIFh1 and NIFh2 (Fig. 3). Estimated particle diameters were found to vary from 2.9 ± 0.6 nm (NIFh1) to 2.6 ± 0.5 nm (NIFh2). Particles appear to be poorly crystalline, and exhibit poorly defined

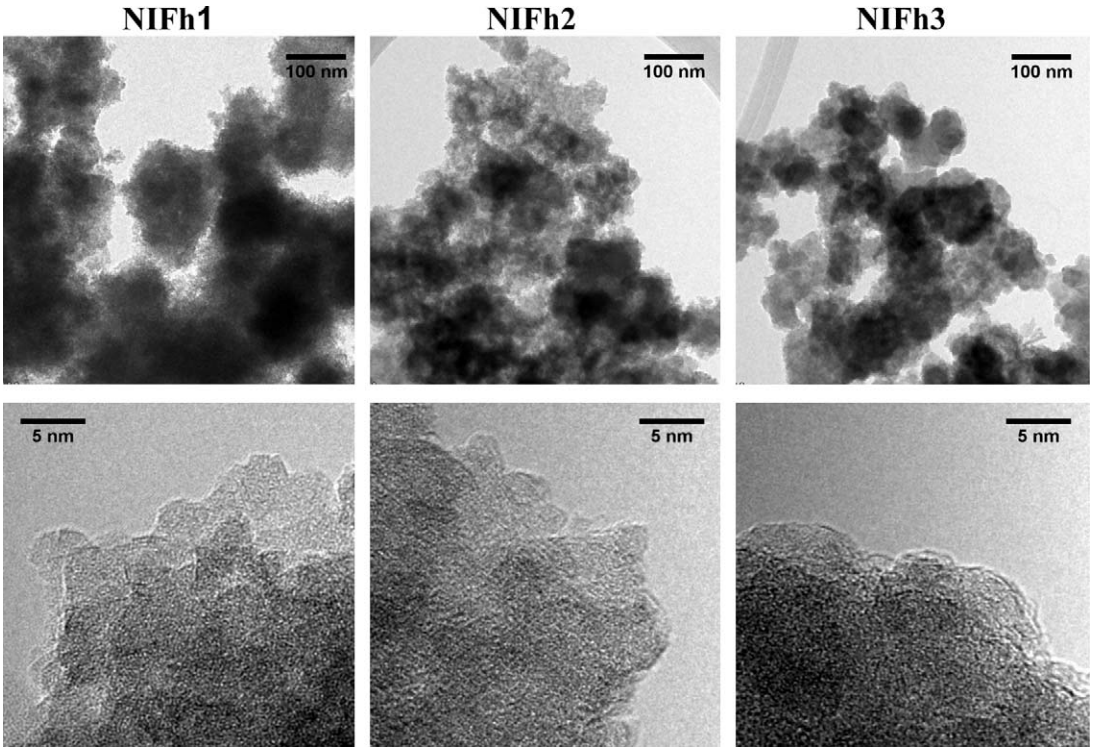

Fig. 3. Transmission Electron Microscopy images of samples NIFh1, NIFh2 and NIFh3, indicate variation in aggregate morphology and ferrihydrite particle sizes.

Fig. 3. Images de microscopie électronique à transmission des échantillons NIFh1, NIFh2 et NIFh3 montrant une variation de la morphologie des agrégats et de la taille des particules de ferrihydrite.

lattice fringes. Sample NIFh3 exhibits particularly poor crystallinity, and individual particles were difficult to discern in this case due to the closely packed appearance of the aggregates. Only a few individual particles of ~2.4 nm were identified at the aggregate edges in some instances. However, this value likely overestimates the actual particle size of this sample.

3.3. Structural aspects of natural ferrihydrite

X-ray diffraction data (Fig. 4) indicate that the New Idria samples exhibit two broad maxima typical of 2-line ferrihydrite, corresponding to d-spacings of 1.4 Å and 2.5 Å and considerable diffuse scattering. In comparison with the XRD pattern of synthetic ferrihydrite, also shown in Fig. 4, the natural samples have broader, less intense maxima, which become progressively weaker from sample NIFh1 to NIFh3. Sharp peaks in these spectra indicate the presence of detrital mineral phases (quartz, albite) and calcite.

Pair distribution functions (PDF) obtained by high-energy X-ray scattering indicate that overall, the short- and intermediate-range ordering of the natural samples are comparable to that of synthetic ferrihydrite (Fig. 5). However, some differences are observed in comparison with the PDF of synthetic ferrihydrite, notably (i) an attenuation of the PDF of the natural samples at lower radial distances, which becomes more pronounced from sample NIFh1 to NIFh3, (ii) differences in relative peak intensities, and (iii) the appearance of new peaks.

The solid arrows in Fig. 5 approximate the radial distances beyond which the PDF signal is reduced to statistical noise. This attenuation in signal represents a good estimate of the extent of structural coherence in materials (Gilbert et al., 2004; Michel et al., 2007b). As such, we estimated the coherent scattering domain (CSD) sizes of the natural ferrihydrites at 18 Å (NIFh1), 15 Å (NIFh2), and 12 Å (NIFh3). The coherent domain size of sample NIFh3 is reduced considerably and is difficult to estimate as a result of the significant statistical noise present even at radial distances of ~8 Å. In comparison, the correlations in the PDF for synthetic 2-line ferrihydrite extend to distances of approximately 20 Å. The error in CSD size estimation is ±3 Å (Hall et al., 2000). The decrease in CSD size is consistent with the increased broadening of the diffraction maxima shown in Fig. 4 and correlates with increasing Al, Si, and organic matter contents.

The association of these species with ferrihydrite is suspected to cause not only a reduction in particle size but also a significant increase in structural disorder. TEM imaging (Fig. 3) provided some visual evidence for a decrease in ferrihydrite particle sizes with increasing impurity contents. However, particle diameters estimated by TEM are consistently larger than the CSD sizes estimated from the PDF data. Such discrepancies between

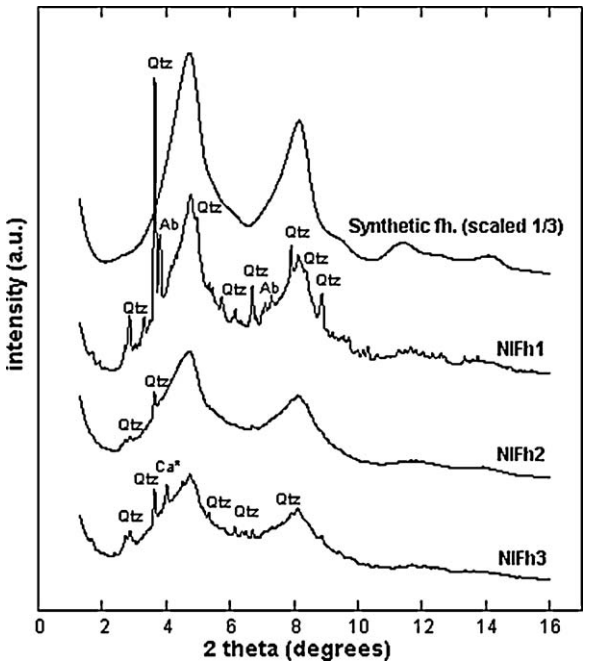

Fig. 4. XRD patterns of natural ferrihydrite samples NIFh1, NIFh2, NIFh3, and synthetic 2-line ferrihydrite collected at ~ 58 keV (λ = 0.212 Å). Selected peaks for quartz (Qtz), albite (Ab) and calcite (Ca) are shown. (*) The $CaCO_3$ polymorph aragonite was found in sample NIFh3 initially; transformation to calcite occurred prior to collection of XRD data shown here.

Fig. 4. Diagrammes de diffraction des rayons-X des échantillons NIFh1, NIFh2, NIFh3 et d'une ferrihydrite synthétique « *2-line* », mesurés à ~ 58 keV (λ = 0,212 Å). Quartz (Qtz), albite (Ab) et calcite (Ca) ont été identifiés. (*) Le polymorphe aragonite a été identifié initialement dans l'échantillon NIFh3; la transformation en calcite a eu lieu avant l'acquisition de ces données.

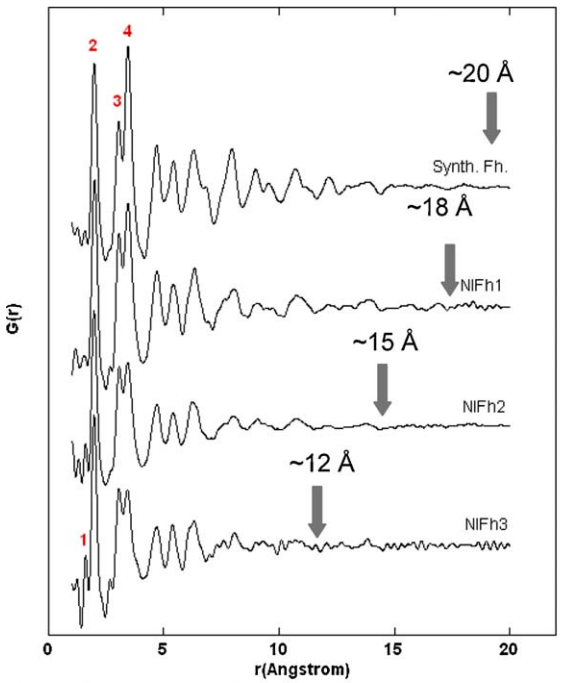

	Distance (Å)	Atom pair
1	1.60	Si-O
2	1.98	Fe-O
3	3.03	Fe-Fe (edge-sharing)
4	3.44	Fe-Fe (corner-sharing)

Figure 5. Pair distribution functions obtained at an energy of ~90 keV (λ = 0.1370 Å) for natural and synthetic 2-line ferrihydrite. Solid arrows indicate approximate radial distances beyond which no atomic correlations typical for ferrihydrite are found, and correspond to coherent scattering domain sizes (± 3 Å). Peak assignments and interatomic distances for the first three major correlations of ferrihydrite are from Michel et al., 2007a (inset table).

Figure 5. Fonctions de distribution de paires mesurées à ~ 90 keV (λ = 0,1370 Å) pour les ferrihydrites naturelles et la ferrihydrite synthétique « *2-line* ». Les flèches indiquent les distances approximatives pour lesquelles les corrélations atomiques correspondant à la ferrihydrite disparaissent; ces distances correspondent à la taille des domaines cohérents de diffusion (± 3 Å). Les paires d'atomes et les distances interatomiques (cf. tableau) correspondant aux trois premiers pics de la ferrihydrite ont été identifiées par Michel et al., 2007a.

particle size and CSD sizes have been attributed to structural disorder (Gilbert et al., 2004, Michel et al., 2007b). Any type of structural disorder, which may be caused by structural strain, relaxation of the surface atoms, ion substitutions, or an increase in vacancies will not result in coherent scattering and may be reflected in the PDF as shifts in peak positions or peak broadening; at higher radial distances this results in an attenuation of the PDF. Furthermore, in the case of compositionally diverse samples shown in this study, additional disorder can be expected from the presence of disordered, compositionally heterogeneous surfaces.

The first three major features in the PDF of synthetic 2-line ferrihydrite were assigned to Fe-O, Fe-Fe edge-sharing, and Fe-Fe corner-sharing distances by Michel et al. (2007a). Interatomic distances for these atom pairs are shown in the inset table of Fig. 5. These atomic pair correlations are present in the PDFs of natural samples at equivalent distances, but some differences in the intensity of atom pair correlations were observed. Specifically, there is a significant reduction in the intensity of the third major correlation (corresponding to Fe-Fe corner-sharing linkages) for samples NIFh2 and NIFh3, which occurs in parallel with the reduction in structural coherence. A similar decrease in corner-sharing Fe-Fe pair correlations has been observed in previous studies on iron precipitates in the presence of strong-binding ligands such as silica (Doelsch et al., 2000), arsenate (Waychunas et al., 1993), and organic ligands (Toner et al., 2009) by means of Fe K-edge EXAFS spectroscopy and has been attributed to a disruption of the ferrihydrite crystallinity.

An indication of compositional variability among the three samples is noted in their PDFs in the form of an additional spectral feature at a slightly shorter distance than the Fe-O distance (~1.6 Å). This feature was attributed to a Si-O atom pair and is found only in the PDFs of samples NIFh2 and NIFh3, which contain significant silica in the poorly crystalline fraction (7.2 and 9.1 wt % for NIFh2 and NIFh3, respectively). We expect that silica

has the strongest effect on the crystallinity/particle size of the New Idria ferrihydrites as a result of its abundance and its strong interaction with ferric oxyhydroxide polymers during precipitation (see, e.g., Pokrovski et al., 2003). Silica was suggested to hinder growth of ferrihydrite crystallites by attaching to newly formed iron oligomers during polymerization and by inhibiting the cross-linking of edge-sharing Fe oligomers. At higher concentrations, silica is thought to polymerize and form a shell around the ferric hydrous oxide core (Seehra et al., 2004). Similarly, a natural siliceous ferrihydrite was described by an analogous model, in which surface-bound silica bridges ferrihydrite-like cores or domains (Parfitt et al., 1992). It is possible that similar mechanisms were responsible for the formation of the New Idria precipitates in the presence of silica. Silica may thus be surface-bound, either in the form of surface complexes or precipitates. Chemical substitution of silica in ferrihydrite should be very limited because of the considerable difference in ionic radii between Si^{4+} and Fe^{3+} (0.26 Å for $^{IV}Si^{4+}$ and 0.49 Å for $^{IV}Fe^{3+}$ (Shannon, 1976) and the limited number of tetrahedral sites in the average ferrihydrite structure (ideally 20% of the total Fe sites). Although NOM is not as abundant as silica in these samples, its presence may also contribute to a decrease in ferrihydrite crystallinity through a similar surface poisoning process; it has been shown that even small amounts of NOM present during precipitation can affect the particle size as well as the structural order of ferrihydrite (Eusterhues et al., 2008; Mikutta et al., 2008).

Aluminum is not expected to affect ferrihydrite crystallinity to the same extent as silicon. Al^{3+} is known to substitute for ferric iron in most crystalline iron oxides, as a result of similar ionic radii and charge (0.54 Å for $^{VI}Al^{3+}$ vs. 0.65 Å for $^{VI}Fe^{3+}$). Previous studies have shown that synthetic 2-line ferrihydrite can accommodate up to ~80 mol% Al (Harvey and Rhue, 2008), although currently there is no definitive proof for structural incorporation of this level of Al^{3+} through true chemical substitution. However, broadening of X-ray diffraction maxima of synthetic aluminous ferrihydrites and an observed distortion of iron octahedral environments shown by Mössbauer spectroscopy point to an intimate association of Al with synthetic ferrihydrite (Chadwick et al., 1986). In principle, Al could substitute for either the octahedral or tetrahedral Fe sites in the ferrihydrite structure, as was shown for other $^{IV}Fe^{3+}$-bearing iron oxides such as maghemite (Wolska and Schwertmann, 1989); in this case, Al substitution was also found to destroy vacancy ordering in maghemite. It may be possible that Al incorporation in the New Idria ferrihydrites causes additional structural disorder, reflected by the attenuation of their PDFs, as a result of distortion of Fe sites or an increase in vacancies or vacancy disorder.

4. Conclusions

Despite considerable variability in composition, we have shown that overall, the short- and intermediate-range atomic ordering of ferrihydrite are preserved in naturally occurring samples to radial distances up to 18 Å. However, X-ray scattering data indicate that structural coherence decreases with increasing Al, Si, and NOM contents. Structural disorder could be caused by an increase in structural strain, which may be due to a decrease in particle size induced by silica (or organic matter) surface poisoning, to chemical substitutions in the ferrihydrite structure (e.g., Al), to an increase in vacancies or vacancy disorder, or to the presence of strained or compositionally different nanoparticle surfaces. We expect the surface reactivity of these ferrihydrites to be affected significantly by the presence of Al, Si, and NOM as a result of variability in their surface composition, particle size and aggregation properties, and a study of such effects is currently underway.

Acknowledgments

This study was supported by NSF Grant CHE-0431425 (Stanford Environmental Molecular Science Institute), NSF Grant EF-0830093 (Center for Environmental Implications of Nanotechnology), the DOE-Office of Biological and Environmental Research through the Science Focus Area at the Stanford Synchrotron Radiation Lightsource, SLAC National Accelerator Laboratory, Stanford University, and the Corning Inc. Foundation. We wish to thank Peter Chupas and Evan Maxey (APS) for technical support on APS BL ID-11-B, Anne Marshall (Stanford University) for help with TEM image acquisition, and Guangchao Li (Stanford University) for ICP-AES analyses.

References

Anderson, P.R., Benjamin, M.M., 1985. Effects of silicon on the crystallization and adsorption properties of ferric oxides. Environ. Sci. Technol. 19, 1048–1053.

Anderson, P.R., Benjamin, M.M., 1990. Surface and bulk characteristics of binary oxide suspensions. Environ. Sci. Technol. 24, 692–698.

Benzerara, K., Yoon, T.H., Tyliszczak, T., Constantz, B., Spormann, A.M., Brown Jr., G.E., 2004. Scanning transmission x-ray microscopy study of microbial calcification. Geobiol. 2, 249–259.

Bluhm, H., Andersson, K., Araki, T., Benzerara, K., Brown, G.E., Dynes, J.J., Ghosal, S., Gilles, M.K., Hansen, H.C., Hemminger, J.C., Hitchcock, A.P., Ketteler, G., Kilcoyne, A.L.D., Kneedler, E., Lawrence, J.R., Leppard, G.G., Majzlan, J., Mun, B.S., Myneni, S.C.B., Nilsson, A., Ogasawara, H., Ogletree, D.F., Pecher, K., Salmeron, M., Shuh, D.K., Tonner, B., Tyliszczak, T., Warwick, T., Yoon, T.H., 2006. Soft X-ray microscopy and spectroscopy at the molecular environmental science beamline at the Advanced Light Source. J. Electron. Spectrosc. 150, 86–104.

Boyd, T., Scott, S.D., 1999. Two-XRD-line ferrihydrite and Fe-Si-Mn oxyhydroxide mineralization from Franklin Seamount, western Woodlark basin, Papua New Guinea. Can. Mineral. 37, 973–990.

Carlson, L., Schwertmann, U., 1981. Natural ferrihydrites in surface deposits from Finland and their association with silica Geochim. Cosmochim. Acta 45, 421–429.

Chadwick, J.C., Jones, D.H., Thomas, M.F., Tatlock, G.J., Devenish, R.W., 1986. A Mössbauer study of ferrihydrite and aluminium substituted ferrihydrites. J. Magnetism Magnetic Mater. 61, 88–100.

Chan, C.S., De Stasio, G., Welch, S.A., Girasole, M., Frazer, B.H., Nesterova, M.V., Fakra, S., Banfield, J.F., 2004. Microbial polysaccharides template assembly of nanocrystal fibers. Science 303, 1656–1658.

Childs, C.W., Downes, C.J., Wells, N., 1982. Hydrous Iron Oxide Minerals with Short Range Order Deposited in a Spring/Stream System, Tongariro National Park, New Zealand. Aust. J. Soil. Res. 20, 119–129.

Chupas, P.J., Qiu, X., Hanson, J.C., Lee, P.L., Grey, C.P., Billinge, S.J.L., 2003. Rapid-acquisition pair distribution function (RA-PDF) analysis. J. Appl. Cryst. 36, 1342–1347.

Combes, J.M., Manceau, A., Calas, G., 1989. Formation of ferric oxides from aqueous solutions: a polyhedral approach by X-ray absorption spectroscopy: I. Hydrolysis and formation of ferric gels. Geochim. Cosmochim. Acta 53, 583–594.

Combes, J.M., Manceau, A., Calas, G., 1990. Formation of ferric oxides from aqueous solutions: a polyhedral approach by X-ray Absorption Spec-

troscopy: II. Hematite formation from ferric gels. Geochim. Cosmochim. Acta 54, 1083–1091.
Doelsch, E., Masion, A., Bottero, J.Y., Nahon, D., Bertsch, P.M., 2000. Speciation and Crystal Chemistry of Iron (III) Chloride Hydrolyzed in the Presence of SiO_4 Ligands 1. An Fe K-Edge EXAFS Study. Langmuir, 4726–4731.
Drits, V.A., Sakharov, B.A., Salyn, A.L., Manceau, A., 1993. Structural model for ferrihydrite. Clay Minerals 28, 185–208.
Ehm, L., Antao, S.M., Chen, J., Locke, D.R., Michel, F.M., Martin, C.D., Yu, T., Parise, J.B., Lee, P.L., Chupas, P.J., Shastri, S.D., Guo, Q., 2007. Studies of local and intermediate range structure in crystalline and amorphous materials at high pressure using high-energy X-rays. Powder Diffrac. 22, 108–112.
Eusterhues, K., Wagner, F.E., Hausler, W., Hanzlik, M., Knicker, H., Totsche, K.U., Kogel-Knabner, I., Schwertmann, U., 2008. Characterization of ferrihydrite-soil organic. Matter coprecipitates by X-ray diffraction and mössbauer spectroscopy. Environ. Sci. Technol 42, 7891–7897.
Ferris, F.G., Tazaki, K., Fyfe, W.S., 1989. Iron oxides in acid mine drainage environments and their association with bacteria. Chem. Geol. 74, 321–330.
Fortin, D., Leppard, G.G., Tessier, A., 1993. Characteristics of lacustrine diagenetic iron oxyhydroxides. Geochim. Cosmochim. Acta 57, 4391–4404.
Gilbert, B., Huang, F., Zhang, H., Waychunas, G.A., Banfield, J.F., 2004. Nanoparticles: Strained and Stiff. Science 305, 651–654.
Hall, B.D., Zanchet, D., Ugarte, D., 2000. Estimating nanoparticle size from diffraction measurements. J. Appl. Cryst. 33, 1335–1341.
Hammersley, A.P., 1998. Fit2D V9.129 Reference Manual V. 3.1; ESRF Internal Report ESRF98HA01 T. European Synchrotron Radiation Facility, Grenoble, France, 306 p.
Harvey, O.R., Rhue, R.D., 2008. Kinetics and energetics of phosphate sorption in a multi-component Al (III)–Fe (III) hydr(oxide) sorbent system. J. Colloid Interf. Sci. 322, 384–393.
Henmi, T., Wells, N., Childs, C.W., Parfitt, R.L., 1980. Poorly-ordered iron-rich precipitates from springs and streams on andesitic volcanos. Geochim. Cosmochim. Acta 44, 365–372.
Hitchcock, A.P., 2000. AXis2000 software (ver2.1n) , http://unicorn.mcmaster.ca/aXis2000.html.
Hitchcock, A.P., 2001. Chemical mapping with soft X-ray spectro-microscopy. Am. Lab. 33, 30–36.
Jambor, J.L., Dutrizac, J.E., 1998. Occurrence and constitution of natural and synthetic ferrihydrite, a widespread iron oxyhydroxide. Chem. Rev. 98, 2549–2585.
Jentzsch, T.L., Penn, R.L., 2006. Influence of aluminum doping on ferrihydrite nanoparticle reactivity. J. Phys. Chem. B 110, 11746–11750.
Kennedy, C.B., Scott, S.D., Ferris, F.G., 2003. Characterization of bacteriogenic iron oxide deposits from axial volcano, Juan de Fuca Ridge. Northeast Pacific Ocean. Geomicrobiol. J. 20, 199–214.
Kim, J.J., Kim, S.J., 2003. Environmental, mineralogical, and genetic characterization of ochreous and white precipitates from acid mine drainages in Taebaeg, Korea. Environ. Sci. Technol. 37, 2120–2126.
Loeppert, R.H., Inskeep, W.P., 1996. Iron. In: Sparks, D.L. (Ed.), Methods of soil analysis. Part 3 – chemical methods, Soil Science Society of America Inc, Madison, USA, pp. 639–664.
Majzlan, J., Lalinska, B., Chovan, M., Jurkovic, L., Milovska, S., Göttlicher, J., 2007. The formation, structure, and ageing of As-rich hydrous ferric oxide at the abandoned Sb deposit Pezinok (Slovakia). Geochim. Cosmochim. Acta 71, 4206–4220.
Manceau, A., 2009. Evaluation of the structural model for ferrihydrite derived from real-space modelling of high-energy X-ray diffraction data. Clay Minerals 44, 19–34.
Manceau, A., 2010. PDF analysis of ferrihydrite and the violation of Pauling's Principia. Clay Minerals 45, 225–228.
Masue, Y., Loeppert, R.H., Kramer, T.I., 2007. Arsenate and arsenite adsorption and desorption behavior on coprecipitated aluminum: iron hydroxides. Environ. Sci. Technol. 41, 837–842.
Michel, F.M., Ehm, L., Antao, S.M., Lee, P.L., Chupas, P.J., Liu, G., Strongin, D.R., Schoonen, M.A.A., Phillips, B.L., Parise, J.B., 2007a. The structure of ferrihydrite, a nanocrystalline material. Science 316, 1726–1729.
Michel, F.M., Ehm, L., Liu, G., Han, W.Q., Antao, S.M., Chupas, P.J., Lee, P.L., Knorr, K., Eulert, H., Kim, J., Grey, C.P., Celestian, A.J., Gillow, J., Schoonen, M.A.A., Strongin, D.R., Parise, J.B., 2007b. Similarities in 2- and 6-line ferrihydrite based on pair distribution function analysis of X-ray total scattering. Chem. Mater 35, 1489–1496.
Michel, F.M., Barrón, V., Torrent, J., Morales, A.P., Serna, C.J., Boily, J.-F., Liu, Q., Ambrosini, A., Cismasu, A.C., Brown, G.B., 2010. Ordered ferrimagnetic form of ferrihydrite reveals links among structure, composition, and magnetism. Proc. Nat. Acad. Sci. 107, 2787–2792.
Midwood, A.J., Boutton, T.W., 1998. Soil carbonate decomposition by acid has little effect on the δ^{13}C or organic matter. Soil Biol. Biochem. 30, 1301–1307.
Mikutta, C., Kretzschmar, R., 2008. Synthetic coprecipitates of exopolysaccharides and ferrihydrite. Part II: Siderophore-promoted dissolution. Geochim. Cosmochim. Acta 72, 1128–1142.
Mikutta, C., Mikutta, R., Bonneville, S., Wagner, F., Voegelin, A., Christl, I., Kretzschmar, R., 2008. Synthetic coprecipitates of exopolysaccharides and ferrihydrite. Part I: Characterization. Geochim. Cosmochim. Acta 72, 1111–1127.
Parfitt, R.L., van der Gaast, S.J., Childs, C.W., 1992. A structural model for natural siliceous ferrihydrite. Clay Clay Minerals 40, 675–681.
Pichler, T., Veizer, J., Hall, G.E., 1999. Natural input of arsenic into a coral-reef ecosystem by hydrothermal fluids and its removal by Fe(III) oxyhydroxides. Environ. Sci. Technol. 33, 1373–1378.
Pokrovski, G.S., Shott, J., Farges, F., Hazemann, J.-L., 2003. Iron (III)-silica interactions in aqueous solution: insights from X-ray absorption fine structure spectroscopy. Geochim. Cosmochim. Acta 67, 3559–3573.
Qiu, X., Thompson, J.W., Billinge, S.J.L., 2004. *PDFgetX2*: a GUI-driven program to obtain the pair distribution function from X-ray powder diffraction data. J. Appl. Cryst 37, 678.
Rancourt, D.G., Meunier, J.F., 2008. Constraints on structural models of ferrihydrite as a nanocrystalline material. Am. Mineral 93, 1412–1417.
Rytuba, J.J., 2000. Mercury mine drainage and processes that control its environmental impact. Sci. Total Environ. 260, 57–71.
Schumacher, M., Christl, I., Scheinost, A.C., Jacobsen, C., Kretzschmar, R., 2005. Chemical heterogeneity of organic soil colloids investigated by scanning transmission X-ray microscopy and C-1 s NEXAFS microspectroscopy. Environ. Sci. Technol 39, 9094–9100.
Schwertmann, U., Cornell, R.M., 1991. Iron Oxides in the Laboratory. VCH, Weinheim, Germany, 137 p.
Schwertmann, U., Wagner, F., Knicker, H., 2005. Ferrihydrite–humic associations: magnetic hyperfine interactions. Soil Sci. Soc. Am. J. 69, 1009–1015.
Seehra, M.S., Roy, P., Raman, A., Manivannan, A., 2004. Structural investigations of synthetic ferrihydrite nanoparticles doped with Si. Solid State Comm. 130, 597–601.
Shannon, R.D., 1976. Revised effective ionic radii and systematic studies of interatomic distances in halides and chalcogenides. Acta Crystallogr. A 32, 751–767.
Solomon, D., Lehmann, J., Kinyangi, J., Liang, B.Q., Heymann, K., Dathe, L., Hanley, K., Wirick, S., Jacobsen, C., 2009. Carbon (1 s) NEXAFS spectroscopy of biogeochemically relevant reference organic compounds. Soil Sci. Soc. Am. J. 73, 1817–1830.
Tang, Y., Michel, F.M., Zhang, L., Harrington, R., Parise, J.B., Reeder, R.J., 2010. Structural properties of the Cr(III) – Fe(III) (oxy)hydroxide compositional series: insights for a nanomaterial "solid solution". Chem. Mater. 22, 3589–3598.
Toner, B.M., Santinelli, C.M., Marcus, M.A., Wirth, R., Chan, C.S., McCollom, T., Bach, W., Edwards, K.J., 2009. Biogenic iron oxyhydroxide formation at mid-ocean ridge hydrothermal vents: Juan de Fuca Ridge. Geochim. Cosmochim. Acta 73, 388–403.
Waychunas, G.A., Rea, B.A., Fuller, C.C., Davis, J.A., 1993. Surface chemistry of ferrihydrite: Part I: EXAFS studies of the geometry of coprecipitated and adsorbed arsenate. Geochim. Cosmochim. Acta 57, 2251–2269.
Wolska, E., Schwertmann, U., 1989. The vacancy ordering and distribution of aluminium ions in γ-$(FeAl)_2O_3$. Solid State Ionics 33, 214–218.